COMM. MATH. SCI.
Vol. 13, No. 6, pp. 1615–1638

MACROSCOPIC MODELS OF COLLECTIVE MOTION WITH REPULSION *

PIERRE DEGOND †, GIACOMO DIMARCO ‡, THI BICH NGOC MAC §, AND NAN WANG ¶

Abstract. We study a system of self-propelled particles which interact with their neighbors via alignment and repulsion. The particle velocities result from self-propulsion and repulsion by close neighbors. The direction of self-propulsion is continuously aligned to that of the neighbors, up to some noise. A continuum model is derived starting from a mean-field kinetic description of the particle system. It leads to a set of non conservative hydrodynamic equations. We provide a numerical validation of the continuum model by comparison with the particle model. We also provide comparisons with other self-propelled particle models with alignment and repulsion.

Key words. Fokker–Planck equation, macroscopic limit, Von Mises–Fisher distribution, generalized collision invariants, non-conservative equations, self-organized hydrodynamics, self-propelled particles, alignment, repulsion.

AMS Subject classification: 35Q80, 35L60, 82C22, 82C70, 92D50.

1. Introduction

The study of collective motion in systems consisting of a large number of agents, such as bird flocks, fish schools, suspensions of active swimmers (bacteria, sperm cells), etc. has triggered the creation of an intense amount of literature in recent years. We refer to [32, 21] for recent reviews on the subject. Many such studies rely on a particle model or Individual Based Model (IBM) that describes the motion of each individual separately (see e.g. [2, 6, 7, 8, 9, 18, 22, 24, 29]).

In this work, we aim to describe dense suspensions of elongated self-propelled particles in a fluid, such as sperm. In such dense suspensions, repulsion due to volume exclusion is an essential ingredient of the dynamics. A large part of the literature is concerned with dilute suspensions [19, 21, 25, 28, 33]. In these approaches, the Stokes equation for the fluid is coupled to the orientational distribution function of the self-propelled particles. However, these approaches are of "mean-field type;" i.e., they assume that particle interactions are mediated by the fluid through some kinds of averages. These approaches do not deal easily with short-range interactions, such as repulsion, due to volume exclusion or interactions mediated by lubrication forces. Additionally, these models assume a rather simple geometry of the swimmers, which are reduced to a force dipole, while the true geometry and motion of an actual swimmer, like a sperm cell, is considerably more complex.

In a recent work [26], Peruani et. al. showed that for dense systems of elongated self-propelled particles volume-exclusion interaction results in alignment. Relying on this work, and owing to the fact that the description of swimmer interactions from

*Received: August 18, 2014; accepted (in revised form): July 7, 2014. Communicated by Eitan Tadmor.

†Department of Mathematics, Imperial college London, London SW7 2AZ, United Kingdom (pdegond@imperial.ac.uk).

‡Department of Mathematics, University of Ferrara, 44100 Ferrara, Italy (giacomo.dimarco@unife.it).

§Université de Toulouse; UPS, INSA, UT1, UTM, Institut de Mathématiques de Toulouse, CNRS, Institut de Mathématiques de Toulouse UMR 5219, F-31062 Toulouse, France (thi-bich-ngoc.mac@math.univ-toulouse.fr)

¶National University of Singapore, Department of Mathematics, Lower Kent Ridge Road, Singapore (g0901252@nus.edu.sg)

first physical principles is by far too complex, we choose to replace the fluid-mediated interaction by a simple alignment interaction of Vicsek type [31]. In the Vicsek model, the agents move with constant speed and attempt to align with their neighbors up to some noise. Many aspects of the Vicsek model have been studied, such as phase transitions [1, 6, 10, 11, 17, 31], numerical simulations [23], and derivation of macroscopic models [4, 13].

The alignment interaction acting alone may trigger the formation of high particle concentrations. However, in dense suspensions, volume exclusion prevents such high densities from occuring. When distances between particles become too small, repulsive forces are generated by the fluid or by the direct reaction of the bodies to each other. These forces contribute to repel the particles and to prevent further contacts. To model this behavior, we must add a repulsive force to the Vicsek alignment model. Inspired by [3, 18, 29], we consider the possibility that the particle orientations (i.e. the directions of the self-propulsion force) and the particle velocities may be different. Indeed, volume-exclusion interaction may push the particles in a direction different from that of their self-propulsion force.

We consider an overdamped regime in which the velocity is proportional to the force through a mobility coefficient. The overdamped limit is justified by the fact that the background fluid is viscous and thus the forces due to friction are very large compared to those due to motion. Indeed, for micro-size particles, the Reynolds number is very small ($\sim 10^{-4}$), and thus the effect of inertia can be neglected. Finally, differently from [3, 18, 29], we consider an additional term describing the relaxation of the particle orientation towards the direction of the particle velocity. We also take into account Brownian noise in the orientation dynamics of the particles. This noise may take into account the fluid turbulence, for instance. Therefore, the particle dynamics result from an interplay between relaxation towards the mean orientation of the surrounding particles, relaxation towards the direction of the velocity vector, and Brownian noise. From now on, we refer to the above described model as the Vicsek model with repulsion.

Starting from the above described microscopic dynamical system, we successively derive mean-field equations and hydrodynamic equations. Mean field equations are valid when the number of particles is large and describe the evolution of the one-particle distribution, i.e. the probability for a particle to have a given orientation and position at a given instant of time. Expressing that the spatio-temporal scales of interest are large compared to the agents' scales leads to a singular perturbation problem in the kinetic equation. Taking the hydrodynamic limit (i.e. the limit of the singular perturbation parameter to zero) leads to the hydrodynamic model. Hydrodynamic models are particularly well-suited to systems consisting of a large number of agents and to the observation of the system's large scale structures. Indeed, the computational cost of IBM increases dramatically with the number of agents, but that of hydrodynamic models is independent of it. With IBM, it is also sometimes quite cumbersome to access observables such as order parameters, but these quantities are usually directly encoded into the hydrodynamic equations.

The derivation of hydrodynamic models has been intensely studied by many authors. Many of these models are based on phenomenological considerations [30] or derived from moment approaches and ad-hoc closure relations [3, 4, 27]. The first mathematical derivation of a hydrodynamic system for the Vicsek model was proposed in [13]. We refer to this model as the Self-Organized Hydrodynamic (SOH) model. One of the main contributions of [13] is the concept of "Generalized Collision Invariants" (GCI) which permit the derivation of macroscopic equations for a particle system in spite of a lack

of momentum conservation. The SOH model has been further refined in [12, 16].

Performing the hydrodynamic limit in the kinetic equations associated to the Vicsek model with repulsion leads to the so-called "Self-Organized Hydrodynamics with Repulsion" (SOHR) system. The SOHR model consists of a continuity equation for the density ρ and an evolution equation for the average orientation $\Omega \in \mathbb{S}^{n-1}$ where n indicates the spatial dimension. The average orientation of the fluid at (x,t) represents the total sum of the particles orientations in a small volume around x at time t, normalized to unit norm. More precisely, the model reads

$$\partial_t \rho + \nabla_x \cdot (\rho U) = 0, \tag{1.1}$$

$$\rho \partial_t \Omega + \rho (V \cdot \nabla_x)\Omega + P_{\Omega^\perp} \nabla_x p(\rho) = \gamma P_{\Omega^\perp} \Delta_x (\rho \Omega), \tag{1.2}$$

$$|\Omega| = 1, \tag{1.3}$$

where

$$U = c_1 v_0 \Omega - \mu \Phi_0 \nabla_x \rho, \quad V = c_2 v_0 \Omega - \mu \Phi_0 \nabla_x \rho, \tag{1.4}$$

$$p(\rho) = v_0 d \rho + \alpha \mu \Phi_0 \big((n-1)d + c_2\big) \frac{\rho^2}{2}, \quad \gamma = k_0 \big((n-1)d + c_2\big). \tag{1.5}$$

The coefficients c_1, c_2, v_0, μ, Φ_0, d, α, k_0 are associated to the microscopic dynamics and will be defined later on. The symbol $P_{\Omega^\perp}$ stands for the projection matrix $P_{\Omega^\perp} = \mathrm{Id} - \Omega \otimes \Omega$ of $\mathbb{R}^n$ on the hyperplane $\Omega^\perp$. The SOHR model is similar to the SOH model obtained in [12] but with several additional terms which are consequences of the repulsive force at the particle level. The repulsive force intensity is characterized by the parameter $\mu\Phi_0$. In the case $\mu\Phi_0 = 0$, the SOHR system is reduced to the SOH one.

We first briefly describe the original SOH model. Inserting (1.4) and (1.5) with $\mu\Phi_0 = 0$ into (1.1) and (1.2) leads to

$$\partial_t \rho + c_1 v_0 \nabla_x \cdot (\rho \Omega) = 0, \tag{1.6}$$

$$\rho \partial_t \Omega + c_2 v_0 \rho (\Omega \cdot \nabla_x)\Omega + v_0 d P_{\Omega^\perp} \nabla_x \rho = \gamma P_{\Omega^\perp} \Delta_x (\rho \Omega), \tag{1.7}$$

together with (1.3). This model shares similarities with the isothermal compressible Navier–Stokes (NS) equations. Both models consist of a non linear hyperbolic part supplemented by a diffusion term. Equation (1.6) expresses conservation of mass, and Equation (1.7) is an equation for the mean orientation of the particles. It is not conservative, contrary to the corresponding momentum conservation equation in NS. The two equations are supplemented by the geometric constraint (1.3). This constraint is satisfied at all times as soon as it is satisfied initially. Indeed, owing to the presence of the projection operator $P_{\Omega^\perp}$, dotting (1.7) with Ω, we get (provided that $\rho \neq 0$)

$$\partial_t |\Omega|^2 + c_2 v_0 (\Omega \cdot \nabla_x) |\Omega|^2 = 0,$$

showing that $|\Omega|^2(x,t) = 1$ for all times t as soon as $|\Omega|^2(x,0) = 1$ for all x. A second important difference between the SOH model and NS equations is that the convection velocities for the density and the orientation, $v_0 c_1$ and $v_0 c_2$ respectively, are different while for NS they are equal. That $c_1 \neq c_2$ is a consequence of the lack of Galilean invariance of the model (there is a preferred frame which is that of the fluid). The main consequence is that the propagation of sound waves is anisotropic for this type of fluid [30].

The first main difference between the SOH and the SOHR system is the presence of the terms $\mu\Phi_0 \nabla_x \rho$ in the expressions of the velocities U and V. Inserting this term

in the density equation (1.1) results in a diffusion-like term, $-\mu\Phi_0\nabla_x\cdot(\rho(\nabla_x\rho))$, which avoids the formation of high particle concentrations. This term is similar to the nonlinear diffusion term in porous media models. Similarly, inserting the term $\mu\Phi_0\nabla_x\rho$ in the orientation equation (1.2) results in a convection term in the direction of the gradient of the density. Its effect is to force particles to change direction and move towards regions of lower concentration. The second main difference is the replacement of the linear (with respect to ρ) pressure term $v_0 dP_{\Omega^\perp}\nabla_x\rho$ with a nonlinear pressure $p(\rho)$ in the orientation equation (1.2). The nonlinear part of the pressure enhances the effects of the repulsion forces when concentrations become high.

To further establish the validity of the SOHR model (1.1)–(1.5), we perform numerical simulations and compare them to those of the underlying IBM. To numerically solve the SOHR model, we adapt the relaxation method of [23]. In this method, the unit norm constraint (1.3) is abandonned and replaced by a fully conservative hyperbolic model in which Ω is supposed to be in $\mathbb{R}^n$. However, at the end of each time step of this conservative model, the vector Ω is normalized. Motsch and Navoret showed that the relaxation method provides numerical solutions of the SOH model which are consistent with those of the particle model. The resolution of the conservative model can take advantage of the huge literature on the numerical resolution of hyperbolic conservation laws (here specifically, we use [14]). We adapt the technique of [23] to include the diffusion fluxes. Using these approximations, we numerically demonstrate the good convergence of the scheme for smooth initial data and the consistency of the solutions with those of the particle Vicsek model with repulsion.

The outline of the paper is as follows. In Section 2, we introduce the particle model, its mean field limit, the scaling, and the hydrodynamic limit. In Section 3, we present the numerical discretization of the SOHR model, and in Section 4, we present several numerical tests for the macroscopic model and a comparison between the microscopic and macroscopic models. Section 5 is devoted to our conclusion. Some technical proofs will be given in the appendices.

2. Model hierarchy and main results

2.1. The individual-based model and the mean field limit

We consider a system of N-particles, each of which is described by its position $X_k(t)\in\mathbb{R}^n$, its velocity $v_k(t)\in\mathbb{R}^n$, and its direction $\omega_k(t)\in\mathbb{S}^{n-1}$ where $k\in\{1,\cdots,N\}$, n is the spatial dimension and $\mathbb{S}^{n-1}$ denotes the unit sphere. The particle ensemble satisfies the following stochastic differential equations:

$$\frac{dX_k}{dt}=v_k, \tag{2.1}$$

$$v_k=v_0\omega_k-\mu\nabla_x\Phi(X_k(t),t), \tag{2.2}$$

$$d\omega_k=P_{\omega_k^\perp}\circ(\nu\bar{\omega}(X_k(t),t)\,dt+\alpha v_k\,dt+\sqrt{2D}\,dB_t^k). \tag{2.3}$$

Equation (2.1) simply expresses the spatial motion of a particle of velocity v_k. Equation (2.2) shows that the velocity v_k is composed of two components: a self-propulsion velocity of constant magnitude v_0 in direction ω_k and a velocity proportional to the gradient of a potential $\Phi(x,t)$ with mobility coefficient μ. Equation (2.3) describes the time evolution of the orientation. The first term models the relaxation of the particle orientation towards the average orientation $\bar{\omega}(X_k(t),t)$ of its neighbors with rate ν. The second term models the relaxation of the particle orientation towards the direction of the particle velocity v_k with rate α. Finally, the last term describes standard independent white noises dB_t^k of intensity $\sqrt{2D}$. The symbol $\circ$ reminds us that the equation has to be

understood in the Stratonovich sense. Under this condition and thanks to the presence of $P_{\omega^\perp}$, the orthogonal projection onto the plane orthogonal to ω (i.e $P_{\omega^\perp} = (\mathrm{Id} - \omega \otimes \omega)$ where $\otimes$ denotes the tensor product of two vectors and Id is the identity matrix), the orientation ω_k remains on the unit sphere. We assume that v_0, μ, ν, α, D are strictly positive constants.

The potential $\Phi(x,t)$ is the resultant of binary interactions mediated by the binary interaction potential ϕ. It is given by

$$\Phi(x,t) = \frac{1}{N}\sum_{i=1}^{N} \phi\Big(\frac{|x - X_i|}{r}\Big) \tag{2.4}$$

where the binary repulsion potential $\phi(|x|)$ only depends on the distance. We suppose that $x \mapsto \phi(|x|)$ is smooth (in particular implying that $\phi'(0) = 0$ where the prime denotes the derivative with respect to $|x|$). We also suppose that

$$\phi \geq 0, \qquad \int_{\mathbb{R}^n} \phi(|x|)\, dx < \infty,$$

implying in particular that $\phi(|x|) \to 0$ as $|x| \to \infty$. The quantity r denotes the typical range of ϕ. We consider repulsive potentials such that $\phi' < 0$. Since $\phi \to 0$ as $|x| \to \infty$, we have that $\phi \geq 0$ and $\Phi_0 = \int \phi(|x|)\, dx > 0$. In the numerical test section, we will propose precise expressions for this potential force.

The mean orientation $\bar{\omega}(x,t)$ is defined by

$$\bar{\omega}(x,t) = \frac{\mathcal{J}(x,t)}{|\mathcal{J}(x,t)|}, \qquad \mathcal{J}(x,t) = \frac{1}{N}\sum_{i=1}^{N} K\Big(\frac{|x - X_i|}{R}\Big)\omega_i. \tag{2.5}$$

It is constructed as the normalization of the vector $\mathcal{J}(x,t)$ which sums up all orientation vectors ω_i of all the particles which belong to the range of the "influence kernel" $K(|x|)$. The quantity $R > 0$ is the typical range of the influence kernel $K(|x|/R)$ which is supposed to depend only on the distance. It measures how the mean orientation at the origin is influenced by particles at position x. Here, we assume that $x \to K(|x|)$ is smooth at the origin and compactly supported. For instance, if K is the indicator function of the ball of radius 1, the quantity $\bar{\omega}(x,t)$ computes the mean direction of the particles which lie in the sphere of radius R centered at x at time t.

REMARK 2.1. *(i) In the absence of repulsive force (i.e. $\mu = 0$), the system reduces to the time continuous version of the Vicsek model proposed in [13].*
(ii) The model presented is the so-called overdamped limit of the model consisting of (2.1) and (2.3) and where (2.2) is replaced by

$$\epsilon \frac{dv_k}{dt} = \lambda_1(v_0\omega_k - v_k) - \lambda_2 \nabla_x \Phi(X_k(t),t), \tag{2.6}$$

with $\mu = \lambda_2/\lambda_1$. Taking the limit $\epsilon \to 0$ in (2.6), we obtain (2.2). As already mentioned in the introduction, for microscopic swimmers, this limit is justified by the very small Reynolds number and the very small inertia of the particles.

We now introduce the mean field kinetic equation which describes the time evolution of the particle system in the large N limit. The unknown here is the one particle distribution function $f(x,\omega,t)$ which depends on the position $x \in \mathbb{R}^n$, orientation $\omega \in \mathbb{S}^{n-1}$, and time t. The evolution of f is governed by the following system:

$$\partial_t f + \nabla_x \cdot (v_f f) + \nu \nabla_\omega \cdot (P_{\omega^\perp} \bar{\omega}_f f) + \alpha \nabla_\omega \cdot (P_{\omega^\perp} v_f f) - D\Delta_\omega f = 0, \tag{2.7}$$

$$v_f(x,t) = v_0\omega - \mu \nabla_x \Phi_f(x,t), \tag{2.8}$$

where the repulsive potential and the average orientation are given by

$$\Phi_f(x,t) = \int_{\mathbb{S}^{n-1}\times\mathbb{R}^n} \phi\left(\frac{|x-y|}{r}\right) f(y,w,t)\,dw\,dy, \tag{2.9}$$

$$\bar{\omega}_f(x,\omega,t) = \frac{\mathcal{J}_f(x,t)}{|\mathcal{J}_f(x,t)|}, \tag{2.10}$$

$$\mathcal{J}_f(x,t) = \int_{\mathbb{S}^{n-1}\times\mathbb{R}^n} K\left(\frac{|x-y|}{R}\right) f(y,w,t)\,w\,dw\,dy. \tag{2.11}$$

Equation (2.7) is a Fokker–Planck type equation. The second term on the left-hand side of (2.7) describes particle transport in physical space with velocity v_f and is the kinetic counterpart of Equation (2.1). The third, fourth, and fifth terms describe transport in orientation space and are the kinetic counterparts of Equation (2.3). The alignment interaction is expressed by the third term, and the relaxation force towards the velocity v_f is expressed by the fourth term. The fifth term represents the diffusion due to Brownian noise in orientation space. The projection $P_{\omega^\perp}$ insures that the force terms are normal to ω. The symbols $\nabla_\omega\cdot$ and Δ_ω respectively stand for the divergence of tangent vector fields to $\mathbb{S}^{n-1}$ and the Laplace–Beltrami operator on $\mathbb{S}^{n-1}$. Equation (2.8) is the direct counterpart of (2.2).

Eq. (2.9) is the continuous counterpart of Equation (2.4). Indeed, letting f be the empirical measure

$$f = \frac{1}{N}\sum_{i=1}^{N} \delta_{(x_i(t),\omega_i(t))}(x,\omega)$$

in (2.9) (where $\delta_{(x_i(t),\omega_i(t))}(x,\omega)$ is the Dirac delta at $(x_i(t),\omega_i(t))$) leads to (2.4). Similarly, equations (2.10) and (2.11) are the continuous counterparts of (2.5) (by the same kind of argument). The rigorous convergence of the particle system to the above Fokker–Planck equation (2.7) is an open problem. We recall, however, that the derivation of the kinetic equation for the Vicsek model without repulsion has been done in [5] in a slightly modified context.

2.2. Scaling

In order to highlight the role of the various terms, we first write the system in a dimensionless form. We chose t_0 as unit of time and choose

$$x_0 = v_0 t_0, \qquad f_0 = \frac{1}{x_0^n}, \qquad \phi_0 = \frac{v_0^2 t_0}{\mu},$$

as units of space, distribution function, and potential. We introduce the dimensionless variables

$$\tilde{x} = \frac{x}{x_0}, \qquad \tilde{t} = \frac{t}{t_0}, \qquad \tilde{f} = \frac{f}{f_0}, \qquad \tilde{\phi} = \frac{\phi}{\phi_0},$$

and the dimensionless parameters

$$\breve{R} = \frac{R}{x_0}, \qquad \breve{r} = \frac{r}{x_0}, \qquad \breve{D} = t_0 D, \qquad \breve{\nu} = t_0\nu, \qquad \breve{\alpha} = \alpha x_0.$$

In the new set of variables $(\tilde{x},\tilde{t})$, Equation (2.8) becomes (dropping the tildes and the $\breve{}$ for simplicity)

$$v_f = \omega - \nabla_x \Phi_f(x,t),$$

where f, Φ_f, $\bar{\omega}_f$, and $\mathcal{J}_f$ are still given by (2.8), (2.9), (2.10), and (2.11) (now written in the new variables).

We now define the regime we are interested in. We assume that the ranges R and r of the interaction kernels K and ϕ are both small but with R much larger than r. More specifically, we assume the existence of a small parameter $\varepsilon \ll 1$ such that

$$R = \sqrt{\varepsilon}\hat{R}, \qquad r = \varepsilon \hat{r} \qquad \text{with} \qquad \hat{R}, \hat{r} = \mathcal{O}(1).$$

We also assume that the diffusion coefficient D and the relaxation rate to the mean orientation ν are large and of the same order of magnitude (i.e. $d = D/\nu = \mathcal{O}(1)$), while the relaxation to the velocity α stays of order 1, i.e.

$$\nu = \frac{1}{\varepsilon}, \qquad d = \frac{D}{\nu} = \mathcal{O}(1), \qquad \alpha = \mathcal{O}(1).$$

With these new notations, dropping all 'hats', the distribution function $f^\varepsilon(x,\omega,t)$ (where the superscript ε now higlights the dependence of f upon the small parameter ε) satisfies the following Fokker–Plank equation:

$$\varepsilon\Big(\partial_t f^\varepsilon + \nabla_x \cdot (v^\varepsilon_{f^\varepsilon} f^\varepsilon)\Big) + \nabla_\omega \cdot (P_{\omega^\perp} \bar{\omega}^\varepsilon_{f^\varepsilon} f^\varepsilon) + \varepsilon\alpha \nabla_\omega \cdot (P_{\omega^\perp} v^\varepsilon_{f^\varepsilon} f^\varepsilon) - d\Delta_\omega f^\varepsilon = 0, \tag{2.12}$$

$$v^\varepsilon_f = \omega - \nabla_x \Phi^\varepsilon_f(x,t), \tag{2.13}$$

where the repulsive potential and the average orientation are now given by

$$\Phi^\varepsilon_f(x,t) = \int_{\mathbb{S}^{n-1}\times\mathbb{R}^n} \phi\Big(\frac{|x-y|}{\varepsilon r}\Big) f^\varepsilon(y,w,t)\, dw\, dy,$$

$$\bar{\omega}^\varepsilon_f = \frac{\mathcal{J}^\varepsilon_f(x,t)}{|\mathcal{J}^\varepsilon_f(x,t)|}, \quad \mathcal{J}^\varepsilon_f(x,t) = \int_{\mathbb{S}^{n-1}\times\mathbb{R}^n} K\Big(\frac{|x-y|}{\sqrt{\varepsilon}R}\Big) f^\varepsilon(y,w,t)\, w\, dw\, dy.$$

Now, by Taylor expansion and the fact that the kernels K, ϕ only depend on $|x|$, we obtain (provided that K is normalized to 1 i.e. $\int_{\mathbb{R}} K(|x|)\, dx = 1$)

$$v^\varepsilon_f(x,t) = \omega - \Phi_0 \nabla_x \rho^\varepsilon_f + \mathcal{O}(\varepsilon^2), \tag{2.14}$$

$$\bar{\omega}^\varepsilon_f(x,t) = G^0_f(x,t) + \varepsilon G^1_f(x,t) + \mathcal{O}(\varepsilon^2), \tag{2.15}$$

$$G^0_f(x,t) = \Omega_f(x,t), \quad G^1_f(x,t) = \frac{k_0}{|J_f|} P_{\Omega_f^\perp} \Delta_x J_f,$$

where the coefficients k_0, Φ_0 are given by

$$k_0 = \frac{R^2}{2n} \int_{x\in\mathbb{R}^n} K(|x|)|x|^2 dx > 0, \quad \Phi_0 = \int_{x\in\mathbb{R}^n} \phi(|x|) dx > 0. \tag{2.16}$$

For example, if K is the indicator function of the ball of radius 1, then $k_0 = |\mathbb{S}^{n-1}|/2n(n+2)$ where $|\mathbb{S}^{n-1}|$ is the volume of the sphere $\mathbb{S}^{n-1}$. In the cases $d=2$ and $d=3$, we respectively get $k_0 = \pi/8$ and $k_0 = 2\pi/15$. The local density ρ_f, the local current density J_f, and the local average orientation Ω_f are defined by

$$\rho_f(x,t) = \int_{\mathbb{S}^{n-1}} f(x,w,t)\, dw, \tag{2.17}$$

$$J_f(x,t) = \int_{\omega\in\mathbb{S}^{n-1}} f(x,w,t)\, w\, dw, \quad \Omega_f(x,t) = \frac{J_f(x,t)}{|J_f(x,t)|}. \tag{2.18}$$

More details about this Taylor expansion are given in Appendix A . Let us observe that this scaling, first proposed in [12], is different from the one used in [13] and results in the appearance of the viscosity term at the right-hand side of Equation (1.2).

Finally, if we neglect the terms of order ε^2 and we define the so-called collision operator $Q(f)$ by

$$Q(f) = -\nabla_\omega \cdot (P_{\omega^\perp} \Omega_f f) + d\Delta_\omega f,$$

the rescaled system (2.12), (2.13) can be rewritten as follows:

$$\varepsilon\Big(\partial_t f^\varepsilon + \nabla_x \cdot (v_f^\varepsilon f^\varepsilon) + \alpha \nabla_\omega \cdot (P_{\omega^\perp} v_f^\varepsilon f^\varepsilon) + \nabla_\omega \cdot (P_{\omega^\perp} G^1_{f^\varepsilon} f^\varepsilon)\Big) = Q(f^\varepsilon), \tag{2.19}$$

$$v_{f^\varepsilon}(x,\omega,t) = \omega - \Phi_0 \nabla_x \rho_{f^\varepsilon}, \quad G^1_{f^\varepsilon}(x,t) = \frac{k_0}{|J_{f^\varepsilon}|} P_{\Omega_f^\perp} \Delta_x J_{f^\varepsilon}. \tag{2.20}$$

2.3. Hydrodynamic limit

The aim is now to derive a hydrodynamic model by taking the limit $\varepsilon \to 0$ of system (2.19)–(2.20) where the local density ρ_f, the local current J_f, and the local average orientation Ω_f are defined by (2.17)and (2.18).

We first introduce the von Mises-Fisher (VMF) probability distribution $M_\Omega(\omega)$ of orientation $\Omega \in \mathbb{S}^{n-1}$ defined for $\omega \in \mathbb{S}^{n-1}$ by:

$$M_\Omega(\omega) = Z^{-1} \exp\left(\frac{\omega \cdot \Omega}{d}\right), \qquad Z = \int_{\omega \in \mathbb{S}^{n-1}} \exp\left(\frac{\omega \cdot \Omega}{d}\right) d\omega$$

An important parameter is the flux of the VMF distribution, i.e. $\int_{\omega \in \mathbb{S}^{n-1}} M_\Omega(\omega) \omega d\omega$. By obvious symmetry considerations, we have

$$\int_{\omega \in \mathbb{S}^{n-1}} M_\Omega(\omega)\, \omega\, d\omega = c_1 \Omega,$$

where the quantity $c_1 = c_1(d)$ does not depend on Ω, is such that $0 \le c_1(d) \le 1$, and is given by

$$c_1(d) = \int_{\omega \in \mathbb{S}^{n-1}} M_\Omega(\omega)\, (\omega \cdot \Omega)\, d\omega. \tag{2.21}$$

When d is small, M_Ω is close to a Dirac delta δ_Ω and represents a distribution of perfectly aligned particles in the direction of Ω. When d is large, M_Ω is close to a uniform distribution on the sphere and represents a distribution of almost totally disordered orientations. The function $d \in \mathbb{R}_+ \mapsto c_1(d) \in [0,1]$ is strictly decreasing with $\lim_{d\to 0} c_1(d) = 1$ and $\lim_{d\to\infty} c_1(d) = 0$. Therefore, $c_1(d)$ represents an order parameter which corresponds to perfect disorder when it is close to 0 and perfect alignment order when it is close to 1.

We have following theorem.

THEOREM 2.2. *Let f^ε be the solution of (2.19), (2.20). Assume that there exists f such that*

$$f^\varepsilon \to f \quad \text{as} \quad \varepsilon \to 0, \tag{2.22}$$

pointwise as well as all its derivatives. Then, there exist $\rho(x,t)$ and $\Omega(x,t)$ such that

$$f(x,\omega,t) = \rho(x,t) M_{\Omega(x,t)}(\omega), \tag{2.23}$$

Moreover, the functions $\rho(x,t),\Omega(x,t)$ satisfy the following equations:

$$\partial_t \rho + \nabla_x \cdot (\rho U) = 0, \tag{2.24}$$

$$\rho\big(\partial_t \Omega + (V\cdot\nabla_x)\Omega\big) + P_{\Omega^\perp}\nabla_x p(\rho) = \gamma P_{\Omega^\perp}\Delta_x(\rho\Omega), \tag{2.25}$$

where

$$U = c_1\Omega - \Phi_0\nabla_x\rho, \quad V = c_2\Omega - \Phi_0\nabla_x\rho, \tag{2.26}$$

$$p(\rho) = d\rho + \alpha\Phi_0\big((n-1)d+c_2\big)\frac{\rho^2}{2}, \quad \gamma = k_0\big((n-1)d+c_2\big), \tag{2.27}$$

and the coefficients c_1 and c_2 will be defined in formulas (2.21) and (2.35) below.
Going back to unscaled variables, we obtain the model (1.1)–(1.5) presented in the introduction.

Proof: The proof of this theorem is divided into three steps: (i) determination of the equilibrium states, (ii) determination of the Generalized Collision Invariants, and (iii) computation of the hydrodynamic limit. We give a sketch of the proof for each step.

Step (i): determination of the equilibrium states We define the equilibria as the elements of the null space of Q considered as an operator acting on functions of ω only.

DEFINITION 2.3. *The set $\mathcal{E}$ of equilibria of Q is defined by*

$$\mathcal{E} = \big\{ f \in H^1(\mathbb{S}^{n-1}) \,|\, f \geq 0 \text{ and } Q(f) = 0 \big\}.$$

We have the following lemma.

LEMMA 2.4. *The set $\mathcal{E}$ is given by*

$$\mathcal{E} = \Big\{ \rho M_\Omega(\omega) \,|\, \rho \in \mathbb{R}_+,\, \Omega \in \mathbb{S}^{n-1} \Big\}.$$

For a proof of this lemma, see [13]. The proof relies on writing the collision operator as

$$Q(f) = \nabla_\omega \cdot \Big(M_{\Omega_f} \nabla_\omega \big(\frac{f}{M_{\Omega_f}} \big) \Big).$$

Step (ii): Generalized Collision Invariants (GCI). We begin with the definition of a collision invariant.

DEFINITION 2.1. *A collision invariant (CI) is a function $\psi(\omega)$ such that for all functions $f(\omega)$ with sufficient regularity we have*

$$\int_{\omega\in\mathbb{S}^{n-1}} Q(f)\,\psi\, d\omega = 0.$$

We denote by $\mathcal{C}$ the set of CIs. The set $\mathcal{C}$ is a vector space.
As seen in [13], the space of CIs is one dimensional and spanned by the constants. Physically, this corresponds to conservation of mass during particle interactions. Since energy and momentum are not conserved, we cannot hope for more physical conservations. Thus the set of CIs is not large enough to allow us to derive the evolution of the macroscopic quantities ρ and Ω. To overcome this difficulty, a weaker concept of collision invariant, the so-called "generalized collisional invariant" (GCI), has been

introduced in [13]. To introduce this concept, we first define the operator $\mathcal{Q}(\Omega, f)$ which for a given $\Omega \in \mathbb{S}^{n-1}$ is given by

$$\mathcal{Q}(\Omega, f) = \nabla_\omega \cdot \Big(M_\Omega \nabla_\omega \big(\frac{f}{M_\Omega} \big) \Big).$$

We note that

$$Q(f) = \mathcal{Q}(\Omega_f, f), \tag{2.28}$$

and that for a given $\Omega \in \mathbb{S}^{n-1}$, the operator $f \mapsto \mathcal{Q}(\Omega, f)$ is a linear operator. This leads to the following definition.

DEFINITION 2.2. *Let $\Omega \in \mathbb{S}^{n-1}$ be given. A Generalized Collision Invariant (GCI) associated to Ω is a function $\psi \in H^1(\mathbb{S}^{n-1})$ which satisfies*

$$\int_{\omega \in \mathbb{S}^{n-1}} \mathcal{Q}(\Omega, f)\, \psi(\omega)\, d\omega = 0, \quad \forall f \in H^1(\mathbb{S}^{n-1}) \quad \text{such that} \quad P_{\Omega^\perp} \Omega_f = 0. \tag{2.29}$$

We denote by $\mathcal{G}_\Omega$ the set of GCIs associated to Ω.

The following lemma characterizes the set of generalized collision invariants.

LEMMA 2.3. *There exists a positive function h: $[-1,1] \to \mathbb{R}$ such that*

$$\mathcal{G}_\Omega = \{ C + h(\omega \cdot \Omega) \beta \cdot \omega \text{ with arbitrary } C \in \mathbb{R} \text{ and } \beta \in \mathbb{R}^n \text{ such that } \beta \cdot \Omega = 0 \}.$$

The function h is such that $h(\cos\theta) = \frac{g(\theta)}{\sin\theta}$, and $g(\theta)$ is the unique solution in the space V defined by

$$V = \{ g \,|\, (n-2)(\sin\theta)^{\frac{n}{2}-2} g \in L^2(0,\pi), \quad (\sin\theta)^{\frac{n}{2}-1} g \in H^1_0(0,\pi) \},$$

(denoting by $H^1_0(0,\pi)$ the Sobolev space of functions which are square integrable as well as their derivative and vanish at the boundary) of the problem

$$-\sin^{2-n}\theta\, e^{-\frac{\cos\theta}{d}} \frac{d}{d\theta} \big(\sin^{n-2}\theta\, e^{\frac{\cos\theta}{d}} \frac{dg}{d\theta}(\theta) \big) + \frac{n-2}{\sin^2\theta} g(\theta) = \sin\theta.$$

The set $\mathcal{G}_\Omega$ is a n-dimensional vector space.

For a proof we refer to [13] for $n=3$ and to [16] for general $n \geq 2$. We denote by ψ_Ω the vector GCI

$$\psi_\Omega = h(\omega \cdot \Omega) P_{\Omega^\perp} \omega, . \tag{2.30}$$

We note that, thanks to (2.28) and (2.29), we have

$$\int_{\omega \in \mathbb{S}^{n-1}} Q(f)\, \psi_{\Omega_f}(\omega)\, d\omega = 0, \quad \forall f \in H^1(\mathbb{S}^{n-1}). \tag{2.31}$$

Step (iii): Hydrodynamic limit. In the limit $\varepsilon \to 0$, we assume that (2.22) holds. Then, thanks to (2.19), we have $Q(f) = 0$. In view of Lemma 2.4, this implies that f has the form (2.23). We now need to determine the equations satisfied by ρ and Ω.

For this purpose, we divide Equation (2.19) by ε and integrate it with respect to ω. Writing (2.19) as

$$(\mathcal{T}_1 + \mathcal{T}_2 + \mathcal{T}_3) f^\varepsilon = \frac{1}{\varepsilon} Q(f^\varepsilon), \tag{2.32}$$

where

$$\mathcal{T}_1 f = \partial_t f + \nabla_x \cdot (v_f f), \quad \mathcal{T}_2 f = \alpha \nabla_\omega \cdot (P_{\omega^\perp} v_f f), \quad \mathcal{T}_3 f = \nabla_\omega \cdot (P_{\omega^\perp} G_f^1 f), \tag{2.33}$$

we observe that the integral of $\mathcal{T}_2 f^\varepsilon$ and $\mathcal{T}_3 f^\varepsilon$over ω is zero since it is in divergence form and the integral of the right-hand side of (2.32) is zero since 1 is a CI. The integral of $\mathcal{T}_1 f^\varepsilon$ gives

$$\partial_t \rho_{f^\varepsilon} + \nabla_x \cdot \Big(\int_{\mathbb{S}^{n-1}} f^\varepsilon(x,\omega,t)\, v_{f^\varepsilon}(x,\omega,t)\, d\omega \Big) = 0.$$

We take the limit $\varepsilon \to 0$ and use (2.22) to get Equation (2.24) with

$$U = \int_{\mathbb{S}^{n-1}} \rho(x,t)\, M_{\Omega(x,t)}(\omega)\, v_{\rho M_\Omega}(x,\omega,t)\, d\omega.$$

Using (2.20), we get $v_{\rho M_\Omega}(x,\omega,t) = \omega - \Phi_0 \nabla_x \rho(x,t)$. With (2.21), this leads to the first equation (2.26).

Multiplying (2.32) by $\psi_{\Omega_{f^\varepsilon}}$, integrating with respect to ω, and using (2.31), we get

$$\int_{\mathbb{S}^{n-1}} (\mathcal{T}_1 + \mathcal{T}_2 + \mathcal{T}_3) f^\varepsilon(x,\omega,t)\, \psi_{\Omega_{f^\varepsilon}}(x,\omega,t)\, d\omega = 0.$$

Taking the limit $\varepsilon \to 0$, we get

$$\int_{\mathbb{S}^{n-1}} ((\mathcal{T}_1 + \mathcal{T}_2 + \mathcal{T}_3)(\rho M_\Omega))(x,\omega,t)\, \psi_{\Omega(x,t)}(\omega)\, d\omega = 0. \tag{2.34}$$

This equation describes the evolution of the mean direction Ω. The computations which lead to (2.25) are proved in Appendix B. The coefficient c_2 in (2.25) is defined by

$$c_2(d) = \frac{\langle \sin^2\theta \cos\theta\, h \rangle_{M_\Omega}}{\langle \sin^2\theta\, h \rangle_{M_\Omega}} = \frac{\int_0^\pi \sin^n\theta \cos\theta\, M_\Omega\, h\, d\theta}{\int_0^\pi \sin^n\theta\, M_\Omega\, h\, d\theta}, \tag{2.35}$$

where for any function $g(\cos\theta)$, we denote by $\langle g \rangle$

$$\langle g \rangle_{M_\Omega} = \int_{\omega \in \mathbb{S}^{n-1}} M_\Omega(\omega)\, g(\omega \cdot \Omega)\, d\omega = \frac{\int_0^\pi g(\cos\theta)\, e^{\frac{\cos\theta}{d}} \sin^{n-2}\theta\, d\theta}{\int_0^\pi e^{\frac{\cos\theta}{d}} \sin^{n-2}\theta\, d\theta}.$$

Remark 2.5. *The SOHR model (2.24)–(2.25) can be rewritten as follows:*

$$\partial_t \rho + c_1 \nabla_x \cdot (\rho\Omega) = \Phi_0 \Delta_x \left(\frac{\rho^2}{2} \right),$$
$$\partial_t \Omega + (\bar{V} \cdot \nabla_x)\Omega + P_{\Omega^\perp} \nabla_x h(\rho) = \gamma P_{\Omega^\perp} \Delta_x \Omega,$$

where the vectors $\bar{V}$ and the function $h(\rho)$ are defined by

$$\bar{V} = c_2 \Omega - (\Phi_0 + 2\gamma) \nabla_x \rho, \quad h'(\rho) = \frac{1}{\rho} p'(\rho),$$

and where the primes denote derivatives with respect to ρ. This displays this system as coupled nonlinear advection-diffusion equations.

3. Numerical discretization of the SOHR model In this section, we develop the numerical approximation of the system (2.24)–(2.27) in the two dimensional case. As mentioned above, this system is not conservative because of the geometric constraint $|\Omega|=1$. Weak solutions of non-conservative systems are not unique because jump relations across discontinuities are not uniquely defined. This indeterminacy cannot be waived by means of an entropy inequality, in contrast to the case of conservative systems. In [23], the authors addressed this problem for the SOH model. They showed that the model is a zero-relaxation limit of a conservative system where the velocity Ω is non-constrained (i.e. belongs to $\mathbb{R}^n$). Additionally, they showed that the numerical solutions built from the relaxation system are consistent with those of the underlying particle model, and other numerical solutions built directly from the SOH model are not. Here, we extend this idea to the SOHR model. More precisely, we introduce the following relaxation model (in dimension $n=2$):

$$\partial_t\rho^\eta+\nabla_x\cdot(\rho^\eta U^\eta)=0, \tag{3.1}$$

$$\partial_t(\rho^\eta\Omega^\eta)+\nabla_x\cdot(\rho^\eta V^\eta\otimes\Omega^\eta)+\nabla_x p(\rho^\eta)-\gamma\Delta_x(\rho^\eta\Omega^\eta)=\frac{\rho^\eta}{\eta}(1-|\Omega^\eta|^2)\Omega^\eta, \tag{3.2}$$

$$U^\eta=c_1\Omega^\eta-\Phi_0\nabla_x\rho^\eta,\quad V^\eta=c_2\Omega^\eta-\Phi_0\nabla_x\rho^\eta, \tag{3.3}$$

$$p(\rho^\eta)=d\rho^\eta+\alpha\Phi_0\big(d+c_2\big)\frac{(\rho^\eta)^2}{2},\quad \gamma=k_0\big(d+c_2\big). \tag{3.4}$$

The left-hand sides form a conservative system. We obtain the following proposition.

PROPOSITION 3.1. *The relaxation model (3.1)–(3.4) converges to the SOHR model (2.24)–(2.27) as η goes to zero.*

The proof of Proposition 3.1 is given in Appendix C. This allows us to use well-established numerical techniques for solving the conservative system (i.e. the left-hand side of (3.1) and (3.2)). The scheme we propose relies on a time splitting of step Δt between the conservative part

$$\partial_t\rho^\eta+\nabla_x\cdot(\rho^\eta U^\eta)=0, \tag{3.5}$$

$$\partial_t(\rho^\eta\Omega^\eta)+\nabla_x\cdot(\rho^\eta V^\eta\otimes\Omega)+\nabla_x p(\rho^\eta)-\gamma\Delta_x(\rho^\eta\Omega^\eta)=0, \tag{3.6}$$

and the relaxation part

$$\partial_t\rho^\eta=0, \tag{3.7}$$

$$\partial_t(\rho^\eta\Omega^\eta)=\frac{\rho^\eta}{\eta}(1-|\Omega^\eta|^2)\Omega^\eta. \tag{3.8}$$

System (3.5)–(3.6) can be rewritten in the following form (we omit the superscript η for simplicity):

$$\mathcal{U}_t+(F(\mathcal{U},\mathcal{U}_x))_x+(G(\mathcal{U},\mathcal{U}_y))_y=0,$$

where

$$\mathcal{U}=\begin{pmatrix}\rho\\ \rho\Omega_1\\ \rho\Omega_2\end{pmatrix},\quad F(\mathcal{U},\mathcal{U}_x)=\begin{pmatrix}\rho U_1\\ \rho\Omega_1V_1+p(\rho)-\gamma\partial_x(\rho\Omega_1),\\ \rho\Omega_1V_2-\gamma\partial_x(\rho\Omega_2)\end{pmatrix},$$

$$G(\mathcal{U},\mathcal{U}_y)=\begin{pmatrix}\rho U_2\\ \rho\Omega_2V_1-\gamma\partial_y(\rho\Omega_1)\\ \rho\Omega_2V_2+p(\rho)-\gamma\partial_y(\rho\Omega_2)\end{pmatrix}.$$

We now consider the following numerical scheme where we denote by $\mathcal{U}^*_{i,j}$ the approximation of $\mathcal{U}$ at time $t^{n+1}=(n+1)\Delta t$ and position $x_i=i\Delta x, y_j=j\Delta y$:

$$\mathcal{U}^*_{i,j}=\mathcal{U}^n_{i,j}-\frac{\Delta t}{\Delta x}\{F^n_{i+1/2,j}-F^n_{i-1/2,j}\}-\frac{\Delta t}{\Delta y}\{G^n_{i,j+1/2}-G^n_{i,j-1/2}\},$$

where the numerical flux $F^n_{i+1/2,j}$ is given by

$$F^n_{i+1/2,j}=\frac{F^n(\mathcal{U}^n_{i,j},\mathcal{U}^n_{xi,j})+F^n(\mathcal{U}^n_{i+1,j},\mathcal{U}^n_{x(i+1),j})}{2}-P_2^{i+\frac{1}{2}}\Big(\frac{\partial F}{\partial\mathcal{U}}(\bar{\mathcal{U}}^n_{i,j},\bar{\mathcal{U}}^n_{xi,j})\Big)(\mathcal{U}^n_{i+1,j}-\mathcal{U}^n_{i,j}),$$

with

$$\mathcal{U}^n_{xi,j}=\frac{(\mathcal{U}^n_{i+1,j}-\mathcal{U}^n_{i,j})}{\Delta x},\quad \bar{\mathcal{U}}^n_{i,j}=\frac{\mathcal{U}^n_{i,j}+\mathcal{U}^n_{i+1,j}}{2},\quad \bar{\mathcal{U}}^n_{xi,j}=\frac{\mathcal{U}^n_{xi,j}+\mathcal{U}^n_{x(i+1),j}}{2},$$

and the analogous discretization holds for $G^n_{i,j+\frac{1}{2}}$.

In the above formula, $P_2^{i+\frac{1}{2}}$ is a polynomial of matrices of degree 2 calculated with the eigenvalues of the Jacobian matrices $\dfrac{\partial F}{\partial\mathcal{U}}$ at an intermediate state depending on $(\mathcal{U}^n_{i,j},\mathcal{U}^n_{xi,j})$ and $(\mathcal{U}^n_{i+1,j},\mathcal{U}^n_{x(i+1),j})$ as detailed in [14]. To ensure stability of the scheme, the time step Δt satisfies a Courant–Friedrichs–Lewy (CFL) condition computed as the minimum of the CFL conditions required for the hyperbolic and diffusive parts of the system.

Once the approximate solution of the conservative system is computed, equations (3.7) and (3.8) can be solved explicitly. We solve them in the limit $\eta\to 0$. In this limit, we get

$$\rho^{n+1}=\rho^*,\qquad \Omega^{n+1}=\frac{\Omega^*}{|\Omega^*|}$$

where (ρ^*,Ω^*) is the numerical solution of system (3.5)–(3.6). This ends one step of the numerical scheme for the system (3.1)–(3.2).

4. Numerical tests The goal of this section is to present some numerical solutions of the system (2.24)–(2.27) which validate the numerical scheme proposed in the previous section. We will first perform a convergence test. We then successively compare the solutions obtained with the SOHR model to those computed by numerically solving the individual based model (2.1) in regimes in which the two models should provide similar results. We will finally perform some comparisons between the SOH and the SOHR system to highlight the differences of the two models. We will compare the SOHR model with another way to incorporate repulsion in the SOH model, the so-called DLMP model of [12].

For all the tests, we use the model in uscaled variables as described in the introduction (see (1.1)–(1.5)). The potential kernel ϕ is chosen as

$$\phi(x)=\begin{cases}(|x|-1)^2 & \text{if}\quad |x|\le 1,\\ 0 & \text{if}\quad |x|>1,\end{cases}\tag{4.1}$$

which gives $\Phi_0=\dfrac{\pi}{6}$, and for K, by assumption normalized to 1, we choose the following form:

$$K(|z|)=\begin{cases}\dfrac{1}{\pi} & \text{if}\quad |z|\le 1,\\ 0 & \text{if}\quad |z|>1.\end{cases}$$

This leads to $k_0 = \frac{1}{8}$. The other parameters, which are fixed for all simulations if not otherwise stated, are

$$v_0 = 1,\ \mu = \frac{1}{2},\ \alpha = 1,\ d = 0.1,\ L_x = 10,\ L_y = 10,$$

which, in dimension $n = 2$, lead to (after numerically computing the GCIs and the associated integrals)

$$c_1 = 0.9486,\ c_2 = 0.8486.$$

In the visualization of the results, we will use the angle θ of the vector Ω relative to the x-axis, i.e. $\Omega = (\cos\theta, \sin\theta)$.

4.1. Convergence test The first test is targeted at the validation of the proposed numerical scheme. For this purpose, we investigate the convergence when the space step $(\Delta x, \Delta y)$ tends to $(0,0)$ refining the grid and checking how the error behaves asymptotically. The initial mesh size is $\Delta x = \Delta y = 0.25$ while the time step is $\Delta t = 0.001$. We repeat the computation for $(\frac{\Delta x}{2}, \frac{\Delta y}{2})$, $(\frac{\Delta x}{4}, \frac{\Delta y}{4})$, $(\frac{\Delta x}{8}$, and $\frac{\Delta y}{8})$. The convergence rate is estimated through the measure of the L^1 norm of the error for the vectors $(\rho, \cos\theta)$ by using for each grid the next finer grid as a reference solution. The initial data is

$$\rho_0 = 1, \quad \theta_0(x,y) = \begin{cases} \arctan(\frac{y_1}{x_1}) + \frac{\pi}{2} sign(x_1) \text{ if } x_1 \neq 0, \\ \pi \text{ if } x_1 = 0 \text{ and } y_1 > 0, \\ 0 \text{ if } x_1 = 0 \text{ and } y_1 < 0, \end{cases} \tag{4.2}$$

where

$$x_1 = x - \frac{L_x}{2}, \quad y_1 = y - \frac{L_y}{2}.$$

The boundary conditions are fixed in time on the four sides of the square $(\rho^n, \theta^n) = (\rho_0, \theta_0)$. The error curves for the density and for $\cos\theta$ are plotted in Figure 4.1 as a function of the space step in log-log scale at time $T = 1s$. The slope of the error curves are compared to a straight line of slope 1. From the figure, we observe the convergence of the scheme with accuracy close to 1.

4.2. Comparison between the SOHR and the Vicsek model with repulsion

In this subsection, we validate the SOHR model by comparing it to the Vicsek model with repulsion on two different test cases. We investigate the convergence of the microscopic IBM to the macroscopic SOHR model when the scaling parameter ε tends

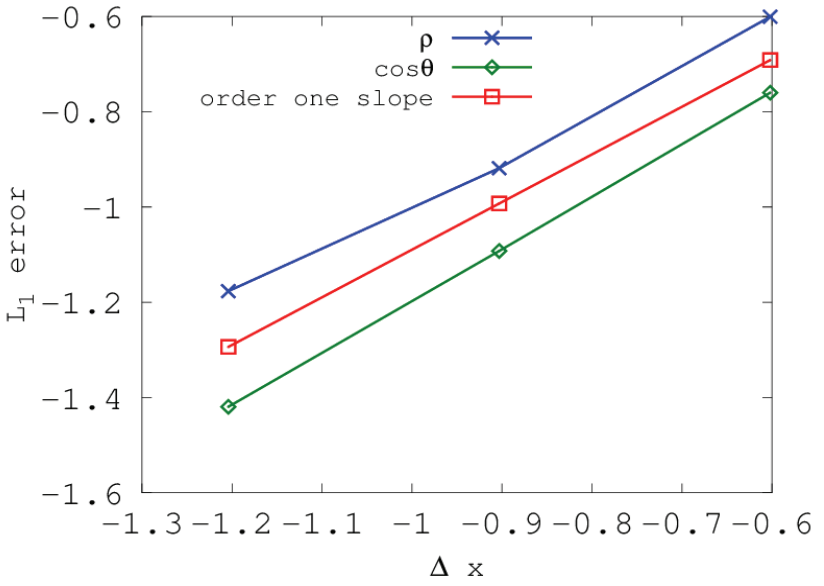

Figure 4.1: L^1-error for the density ρ and the flux direction $\cos\theta$ as a function of Δx in log-log scale. A straight line of slope 1 is plotted for reference. This figure shows that the scheme is numerically of order 1.

to zero. The scaled IBM is written:

$$\frac{dX_k}{dt} = v_k, \qquad v_k = \omega_k - \nabla_x \Phi(X_k(t),t),$$

$$d\omega_k = P_{\omega_k^\perp} \circ \Big(\frac{1}{\varepsilon} \bar{\omega}(X_k(t),t)\, dt + \alpha v_k\, dt + \sqrt{\frac{2d}{\varepsilon}}\, dB_t^k \Big),$$

$$\Phi(x,t) = \frac{1}{\varepsilon^2 N} \sum_{i=1}^{N} \nabla \phi\Big(\frac{|x - X_i|}{\varepsilon r} \Big),$$

$$\bar{\omega}(x,t) = \frac{\mathcal{J}(x,t)}{|\mathcal{J}(x,t)|}, \qquad \mathcal{J}(x,t) = \frac{1}{N} \sum_{i=1}^{N} K\Big(\frac{|x - X_i|}{\sqrt{\varepsilon} R} \Big) \omega_i.$$

The solution of the individual-based model (2.1)–(2.3) is computed by averaging different realizations in order to reduce the statistical errors. The coefficient of the IBM are fixed to $r = 0.0625$ for the repulsive range, $R = 0.25$ for the alignment interaction range, and $N = 10^5$ particles are used for each simulation. The details of the particles simulation can be found in [15, 20] for classical particle approaches or in [23] for a direct application to the SOH model.

Riemann problem: The convergence of the two models is measured as a Riemann problem with the following initial data:

$$(\rho_l, \theta_l) = (0.0067, 0.7), \quad (\rho_r, \theta_r) = (0.0133, 2.3), \tag{4.3}$$

and with periodic boundary condition in x and y. The parameters of the SOHR model are $\Delta t = 0.01$ and $\Delta x = \Delta y = 0.25$. In Figure 4.2 we report the relative L^1 norm of the

error for the macroscopic quantities (ρ,θ) between the SOHR model and the particle model with respect to the number of averages for different values of ε: $\varepsilon=1$ (x-mark), $\varepsilon=0.5$ (plus), $\varepsilon=0.1$ (circle), and $\varepsilon=0.05$ (square) at time $T=1s$. This figure shows, as expected, that the distance between the two solutions diminishes with smaller ε. It seems, however, that the convergence of the error to 0 as $\varepsilon\to 0$ is rather slow. This is due to the fact that for small ε the IBM becomes very stiff. Simultaneously, accuracy is degraded as the interaction region of a particle shrinks to a point which makes the evalution of the average direction of the neighbouring particles very noisy. Since our focus is the continuum model, we did not address this problem which concerns the IBM and did not try to improve the quality of the tests. Indeed, we consider that obtaining the results shown in Figure 4.2 is already quite informative as very few fluid models in the literature are compared with the underlying IBM with such a degree of accuracy.

In Figure 4.3, we report the density ρ and the flux direction θ for the same Riemann problem along the x-axis for $\varepsilon=0.05$ at time $T=1s$, the solution being constant in the y-direction. Again, we clearly observe that the two models provide very close solutions; the small differences are due to the different numerical schemes employed for their discretizations.

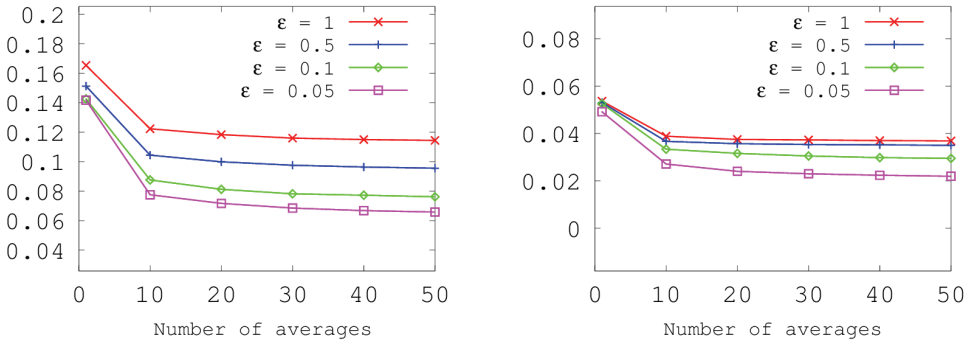

(a) For density ρ (b) For θ

Figure 4.2: Relative error between the macroscopic and the microscopic model for density (a) and θ (b) as a function of the number of averages for different values of ε. The error decreases with both decreasing ε and an increasing number of averages showing that the SOHR model provides a valid approximation of the IBM for ρ and θ.

Taylor–Green vortex problem: In this third test case, we compare the numerical solutions provided by the two models in a more complex case. The initial data are

$$\rho_0=0.01,\quad \Omega_0(x,y)=\frac{\tilde{\Omega}_0(x,y)}{|\tilde{\Omega}_0(x,y)|}, \tag{4.4}$$

where the vector $\tilde{\Omega}_0=(\tilde{\Omega}_{01},\tilde{\Omega}_{02})$ is given by

$$\tilde{\Omega}_{01}(x,y)=\frac{1}{3}\sin(\frac{\pi}{5}x)\cos(\frac{\pi}{5}y)+\frac{1}{3}\sin(\frac{3\pi}{10}x)\cos(\frac{3\pi}{10}y)+\frac{1}{3}\sin(\frac{\pi}{2}x)\cos(\frac{\pi}{2}y),$$
$$\tilde{\Omega}_{02}(x,y)=-\frac{1}{3}\cos(\frac{\pi}{5}x)\sin(\frac{\pi}{5}y)-\frac{1}{3}\cos(\frac{3\pi}{10}x)\sin(\frac{3\pi}{10}y)-\frac{1}{3}\cos(\frac{\pi}{2}x)\sin(\frac{\pi}{2}y),$$

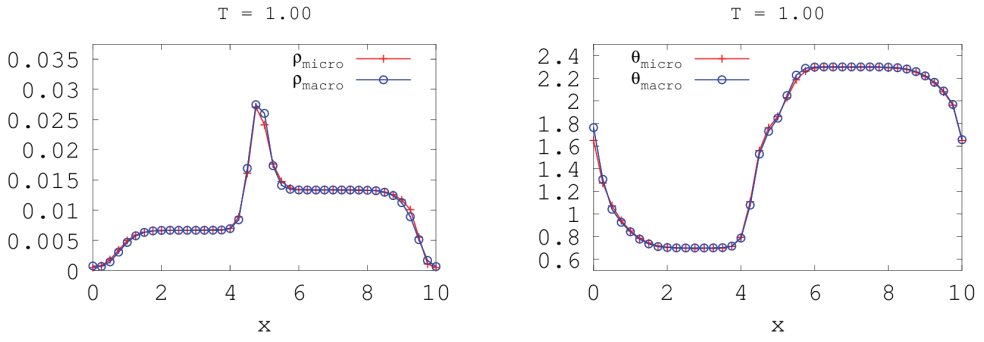

(a) density ρ (b) θ

Figure 4.3: Solution of the Riemann problem (4.3) along the x-axis for the SOHR model (blue line) and for the IBM with $\varepsilon = 0.05$ (red line) at $T = 1s$. The agreement between the two models is excellent. For the SOHR model, the mesh size is $\Delta x = \Delta y = 0.0625$.

with periodic boundary conditions in both directions. The numerical parameters for the SORH model are $\Delta x = \Delta y = 0.2$, and $\Delta t = 0.01$, and for the particle simulations we choose $N = 10^5$ particles, $\varepsilon = 0.05$, $r = 0.04$, and $R = 0.2$. In figures 4.4 and 4.5, we report the density ρ and the flux direction Ω at time $t = 0.6$s. In both figures, the left picture is for the IBM and the right one is for the SOHR model. Again, we find a very good agreement between the two models in spite of the quite complex structure of the solution.

Due to the large number of particles required and the need for averages over a large number of realizations, the IBM is several orders of magnitude more costly than the SOHR model. Indeed, the statistical noise decays like $\mathcal{O}(1/\sqrt{M})$ with the number M of realizations which is very slow. Additionally, the amplitude of the statistical noise increases with time. In practice, we have averaged over up to 100 realizations of the IBM according to the test cases. By contrast, only one single simulation of the SOHR model is needed. Here, we have used an explicit discretization of the diffusion operator because the values of the diffusion constant and of the mesh sizes still led to manageable time steps. In other applications, it could be necessary to perform an implicit discretization of the diffusion operators, but this question is outside the scope of the present work.

In Figure 4.5, we notice that some regions of very small density appear. Since the density equation in the SOHR model exhibits a nonlinearity similar to that of the porous media equation, the density could theoretically become zero in some regions. However, in the simulations presented, we have started from constant density initial data. In this case, we doubt that the solution could become zero in finite time. In the presented simulations, this situation has never occurred and no particular strategy was needed to deal with the zero-density case.

4.3. Comparison between the SOH and the SOHR model In this part, we show the differences between the SOH system (1.6), (1.7) and the SOHR one for different values of the repulsive force Φ_0. The goal is to show that the repulsive effects that the SOHR model adds to the SOH model may have a strong qualitative and quantitative impact on the solution of the models. We recall that the SOHR model reduces to the

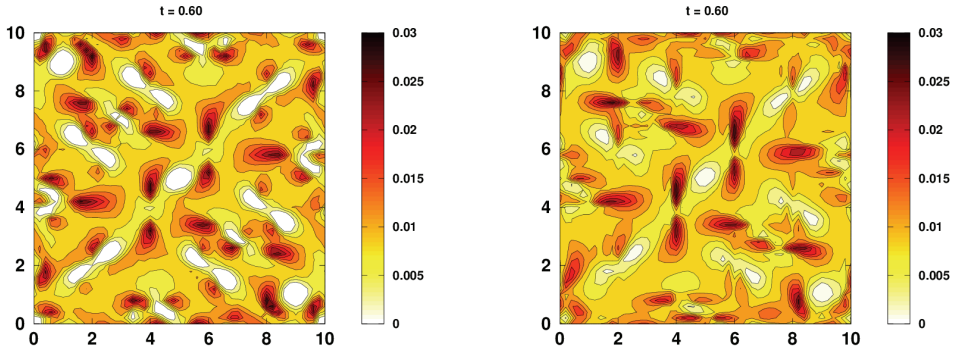

(a) density ρ for the IBM (b) density ρ for the SOHR model

Figure 4.4: Density ρ for the Taylor–Green vortex problem 4.4 at time $t=0.6s$. Left: IBM. Right: SOHR model.

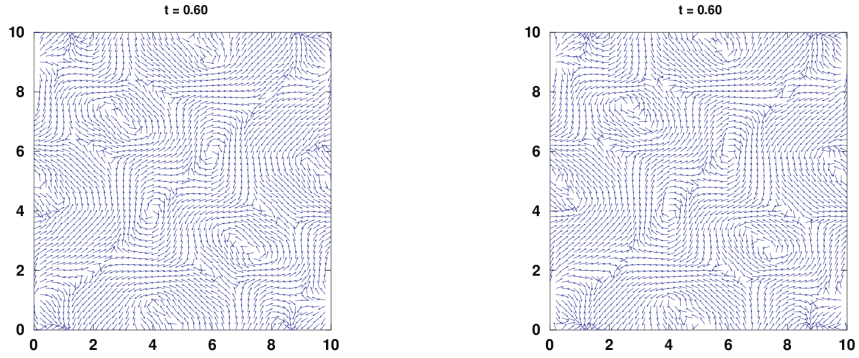

(a) Ω for the IBM (b) Ω for the SOHR model

Figure 4.5: Mean direction Ω for the Taylor–Green vortex problem 4.4 at time $t=0.6s$. Left: IBM. Right: SOHR model.

SOH one in the case where the repulsive force is set equal to zero. To this end, we rescale the repulsive force Φ_0 by

$$\Phi_0 = F_0 \int_{x\in\mathbb{R}^2} \phi(x)dx$$

and let F_0 vary. The repulsive potential ϕ is still given by (4.1) so that $\Phi_0 = F_0\pi/6$. The other numerical parameters are chosen as follows: $d=0.05$, $\alpha=0$, $k_0=1/8$, $\mu=1$, $L_x=10, L_y=10$, $\Delta x=\Delta y=0.15$, and $\Delta t=0.001$. The initial data is that of the vortex problem (4.2) except that we start with four vortices instead of only one. Periodic boundary conditions in both directions are used.

Figure 4.6 displays the solutions for the SOHR system for the density (left) and for the flux direction (right) at $T=1.5s$ with $F_0=5$. Figure (4.7) displays the solutions for $F_0=0.05$. The results are almost indistinguishable from those of the SOH model ($F_0=0$)

and are not shown for this reason. These figures show that when the repulsive force is large enough, the SOHR model can prevent the formation of high concentrations. By contrast, when this force is small, the SOHR model becomes closer to the SOH one, and high concentrations become possible.

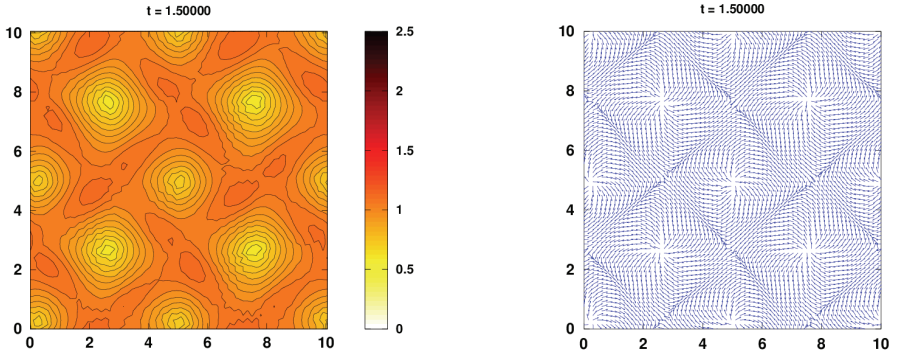

(a) density ρ for $F_0 = 5$ (b) Ω for $F_0 = 5$

Figure 4.6: Solution of the SOHR model for $F_0 = 5$. Density ρ (Figure 4.6a), flux direction Ω (Figure 4.6b) at $t = 1.5s$.

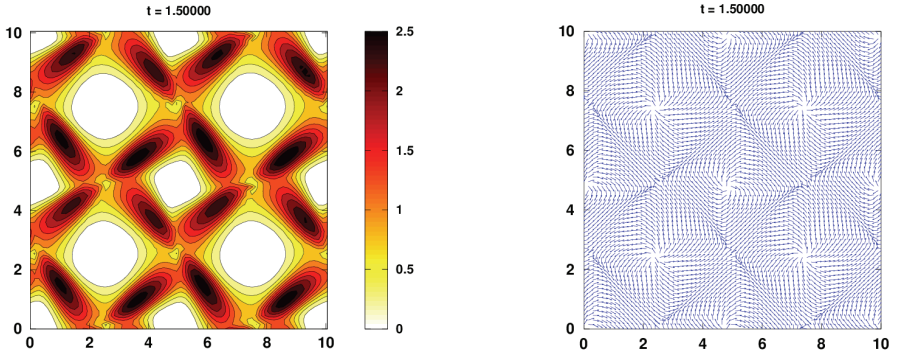

(a) density ρ for $F_0 = 0.05$ (b) Ω for $F_0 = 0.05$

Figure 4.7: Solution of the SOHR model for $F_0 = 0.05$. Density ρ (Figure 4.6a), flux direction Ω (Figure 4.6b) at $t = 1.5s$.

4.4. Comparison between the SOHR and the DLMP model

In this final part, we want to compare the SOHR system to the hydrodynamic model proposed by Degond, Liu, Motsch, and Panferov in [12] (referred to as DLMP model). This model is derived in a similar fashion as the SOHR model, starting from a system of self-propelled particles which obey alignment and repulsion. The main difference is that in the DLMP model the particle velocity is exactly equal to the self-propulsion velocity, but the particles adjust their orientation to respond to repulsion as well as alignment.

The resulting model is of SOH type and is therefore written like (1.6) and (1.7), but with an increased coefficient, $v_0 d(1+\frac{d+c_2}{c_1}F_0)$, in front of the pressure term $P_{\Omega^\perp}\nabla_x\rho$. The initial conditions and numerical parameters are the same as in the previous test.

In Figure 4.8, we report the density ρ (left) and the flux direction Ω (right) for $F_0=5$ for the DLMP model. Comparing Figure (4.6) with Figure 4.8, we observe that the solutions of the SOHR and of the DLMP model are different. The homogenization of the density seems more efficient with the SOHR model than with the DLMP model. This can be attributed to the effect of the nonlinear diffusion terms that are included in the SOHR model but not in the DLMP model. Therefore, the way repulsion is included in the models may significantly affect the qualitative behavior of the solution. In practical situations, when the exact nature of the interactions is unknown, some care must be taken to choose the right repulsion mechanism.

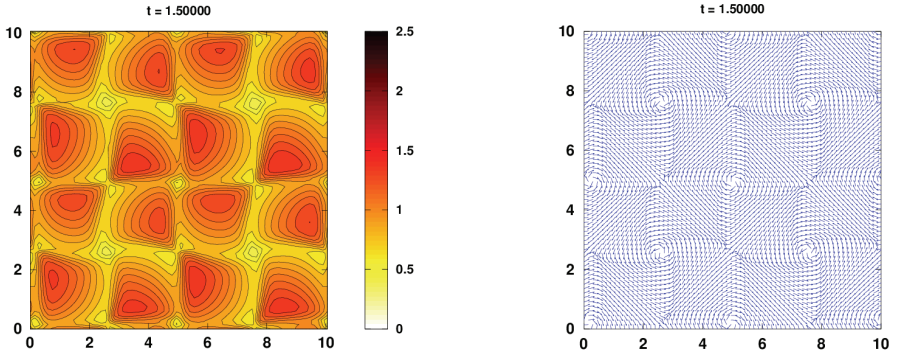

(a) density ρ (b) Ω

Figure 4.8: Solution of the DLMP model for $F_0=5$. Density ρ (left) and flux direction Ω (right) at $t=1.5s$.

5. Conclusion In this paper, we have derived a hydrodynamic model for a system of self-propelled particles which interact through both alignment and repulsion. In the underlying particle model, the actual particle velocity may be different from the self-propulsion velocity as a result of repulsion interactions with the neighbors. Particles update the orientation of their self-propulsion seeking to locally align with their neighbors as in Vicsek alignment dynamics. The corresponding hydrodynamic model is similar to the Self-Organized Hydrodynamic (SOH) system derived from the Vicsek particle model, but it contains several additional terms arising from repulsion. These new terms consist principally of gradients of linear or nonlinear functions of the density including a non-linear diffusion similar to porous medium diffusion. This new Self-Organized Hydrodynamic system with Repulsion (SOHR) has been numerically validated by comparisons with the particle model. It appears more efficient to prevent high density concentrations than other approaches based on simply enhancing the pressure force in the SOH model. In future work, this model will be used to explore self-organized motion in collective dynamics. To this effect, it will be calibrated on data based on biological experiments, such as recordings of collective sperm-cell motion.

Acknowledgement. Pierre Degond is on leave from CNRS, Institut de Mathématiques de Toulouse, France, and Giacomo Dimarco is on leave from Université Paul Sabatier, Institut de Mathématiques de Toulouse, France, where part of this research was conducted. Thi Bich Ngoc Mac wishes to thank the hospitality of the Department of Mathematics, Imperial College London for its hospitality. Nan Wang wishes to thank the Université Paul Sabatier, Institut de Mathématiques de Toulouse, France, for its hospitality. This work has been supported by the French 'Agence Nationale pour la Recherche (ANR)' in the frame of the contract 'MOTIMO' (ANR-11-MONU-009-01).

Appendix A. Proof of formulas (2.14), (2.15). By introducing the change of variable $z=-\dfrac{x-y}{\sqrt{\varepsilon}R}$ and using Taylor expansion, we get

$$\begin{aligned}
&\frac{1}{(\sqrt{\varepsilon}R)^n}\int_{\mathbb{S}^{n-1}\times\mathbb{R}^n} K\big(\frac{|x-y|}{\sqrt{\varepsilon}R}\big)\, f^\varepsilon(y,\omega,t)\omega\, d\omega\, dy\\
&=\int_{\mathbb{S}^{n-1}\times\mathbb{R}^n} K(|z|)\, f^\varepsilon(x+\sqrt{\varepsilon}Rz,\omega,t)\omega\, dz\, d\omega\\
&=\int_{\mathbb{S}^{n-1}\times\mathbb{R}^n} K(|z|)\,\big(f^\varepsilon+\sqrt{\varepsilon}R\nabla_x f^\varepsilon\cdot z+\frac{\varepsilon R^2}{2}D_x^2 f:(z\otimes z)+O(\sqrt{\varepsilon}^3)\big)(x,\omega,t)\omega\, dz\, d\omega\\
&=\big(J(x,t)+\varepsilon k_0\,\Delta_x J(x,t)+O(\varepsilon^2)\big),
\end{aligned}$$

where k_0 is given by (2.16) and $D_x^2 f$ is the Hessian matrix of f with respect to the variable x. Here, we have used that the $\mathcal{O}(\sqrt{\varepsilon})$ and $\mathcal{O}(\varepsilon^{3/2})$ terms vanish after integration in z by oddness with respect to z.

By the same computation for the kernel ϕ, we have

$$\begin{aligned}
&\frac{1}{(\varepsilon r)^n}\int_{\mathbb{S}^{n-1}\times\mathbb{R}^n}\phi(\frac{|x-y|}{\varepsilon r})f^\varepsilon(y,\omega,t)dyd\omega\\
&\qquad=\int_{\mathbb{S}^{n-1}\times\mathbb{R}^n}\phi(|z|)f^\varepsilon(x+\varepsilon rz,\omega,t)dzd\omega\\
&\qquad=\int_{\mathbb{S}^{n-1}\times\mathbb{R}^n}\phi(|z|)(f^\varepsilon+\varepsilon r\nabla_x f\cdot z+O(\varepsilon^2))(x,\omega,t)dzd\omega\\
&\qquad=\Phi_0\int_{\mathbb{S}^{n-1}} f^\varepsilon(x,\omega,t)d\omega+O(\varepsilon^2),
\end{aligned}$$

with $\Phi_0=\int_{\mathbb{R}^n}\phi(|z|)dz$. ∎

Appendix B. Proof of Theorem 2.2 .

We prove that (2.34) leads to (2.25). Thanks to (2.30), Equation (2.34) can be written

$$P_{\Omega^\perp}\int_{\omega\in\mathbb{S}^2}(\mathcal{T}_1(\rho M_\Omega)+\mathcal{T}_2(\rho M_\Omega)+\mathcal{T}_3(\rho M_\Omega))h(\omega\cdot\Omega)\omega d\omega := T_1+T_2+T_3=0, \tag{B.1}$$

where $\mathcal{T}^k$, $k=1,2,3$, are given by (2.33). Now, $\mathcal{T}_1(\rho M_\Omega)$ can be written

$$\mathcal{T}_1(\rho M_\Omega)=\partial_t(\rho M_\Omega)+\nabla_x\cdot(\omega\rho M_\Omega)-\Phi_0\nabla_x\cdot\left(\nabla_x\left(\frac{\rho^2}{2}\right)M_\Omega\right). \tag{B.2}$$

We recall that the first two terms of $\mathcal{T}_1$ on the right hand side of (B.2) and the corresponding terms in T_1 have been computed in [13]. The computation for the third term of $\mathcal{T}_1$ is easy, and we get

$$T_1 = \beta_1 \rho \partial_t \Omega + \beta_2 \rho (\Omega \cdot \nabla_x)\Omega + \beta_3 P_{\Omega^\perp} \nabla_x \rho + \beta_4 (\nabla_x \left(\frac{\rho^2}{2} \right) \cdot \nabla_x)\Omega$$

where the coefficients are given by

$$\beta_1 = \frac{1}{d(n-1)} \langle \sin^2\theta h \rangle_{M_\Omega}, \quad \beta_2 = \frac{1}{d(n-1)} \langle \sin^2\theta \cos\theta h \rangle_{M_\Omega},$$
$$\beta_3 = \frac{1}{n-1} \langle \sin^2\theta h \rangle_{M_\Omega}, \quad \beta_4 = -\frac{\Phi_0}{d(n-1)} \langle \sin^2\theta h \rangle_{M_\Omega}.$$

Now observe that for a constant vector $A \in \mathbb{R}^n$, we have

$$\nabla_\omega (\omega \cdot A) = P_{\omega^\perp} A, \qquad \nabla_\omega \cdot (P_{\omega^\perp} A) = -(n-1)\omega \cdot A. \tag{B.3}$$

Thus, using (2.33), (B.3), and the chain rule, we get for $\mathcal{T}_2(\rho M_\Omega)$

$$\mathcal{T}_2(\rho M_\Omega) = \alpha \Phi_0 \Big((n-1)\omega \cdot \nabla_x \left(\rho^2/2\right) - d^{-1} \nabla_x \left(\rho^2/2\right) \cdot \Omega + d^{-1} \left(\omega \cdot \nabla_x (\rho^2/2)\right)(\omega \cdot \Omega) \Big) M_\Omega.$$

Finally, we obtain

$$T_2 = \beta_5 P_{\Omega^\perp} \nabla_x \left(\frac{\rho^2}{2} \right),$$

where

$$\beta_5 = \alpha \Phi_0 \left(\langle \sin^2\theta h \rangle_{M_\Omega} + \frac{1}{d(n-1)} \langle \sin^2\theta \cos\theta h \rangle_{M_\Omega} \right).$$

The terms $\mathcal{T}_3(\rho M_\Omega)$ and T_3 have been computed in [12]. In particular, it is easy to see that we get them from the formulae for $\mathcal{T}_2(\rho M_\Omega)$ and T_2 by changing $-\alpha \Phi_0 \nabla_x (\rho^2/2)$ into $k_0 P_{\Omega^\perp} \Delta_x (\rho \Omega)$. Therefore, we get

$$T_3 = \beta_6 P_{\Omega^\perp} \Delta_x (\rho \Omega),$$

where

$$\beta_6 = -k_0 \left(\langle \sin^2\theta h \rangle_{M_\Omega} + \frac{1}{d(n-1)} \langle \sin^2\theta \cos\theta h \rangle_{M_\Omega} \right).$$

Inserting the expressions of T_1, T_2 and T_3 into (B.1) we get (2.25). ∎

Appendix C. Proof of Proposition 3.1 .

We follow the lines of the proof of Proposition 3.1 of [23]. Assume that $\rho^\eta \to \rho^0$ and $\Omega^\eta \to \Omega^0$ as η tends to zero. Then, set

$$R^\eta := \rho^\eta (1 - |\Omega^\eta|^2) \Omega^\eta.$$

Multiplying equation (3.2) by η and then taking the limit $\eta \to 0$ yields $R^\eta \to 0$. It follows that $|\Omega^0|^2 = 1$. Since the vector R^η is parallel to Ω^η, we have $P_{(\Omega^\eta)^\perp} R^\eta = 0$ which implies that

$$P_{(\Omega^\eta)^\perp}\Big(\partial_t(\rho^\eta\Omega^\eta) + \nabla_x\cdot(\rho^\eta V^\eta \otimes \Omega^\eta) + \nabla_x p(\rho^\eta) - \gamma\Delta_x(\rho^\eta\Omega^\eta)\Big) = 0.$$

Therefore, letting $\eta \to 0$, we obtain

$$\partial_t(\rho^0\Omega^0) + \nabla_x\cdot(\rho^0 V^0 \otimes \Omega^0) + \nabla_x p(\rho^0) - \gamma\Delta_x(\rho^0\Omega^0) = \beta\Omega^0, \tag{C.1}$$

where β is a real number, $p(\rho^\eta) \to p(\rho^0) = d\rho^0 + \alpha\Phi_0(d+c_2)(\rho^0)^2/2$, $V^0 = c_2\Omega^0 - \Phi_0\nabla_x\rho^0$, and $U^0 = c_1\Omega^0 - \Phi_0\nabla_x\rho^0$. By taking the scalar product of (C.1) with Ω^0, we get

$$\beta = \partial_t\rho^0 + \nabla_x\cdot(\rho^0 V^0) + \nabla_x p(\rho^0)\cdot\Omega^0 - \gamma\Delta_x(\rho^0\Omega^0)\cdot\Omega^0.$$

Inserting this expression of β into (C.1), we find the equation for the evolution of the average direction (2.25) and thus the SOHR model (2.24)–(2.27). ∎

REFERENCES

[1] M. Aldana, V. Dossetti, C. Huepe, V.M. Kenkre, and H. Larralde, *Phase transitions in systems of self-propelled agents and related network models*, Phys. Rev. Lett., 98, 095702, 2007.

[2] I. Aoki, *A simulation study on the schooling mechanism in fish*, B. Jpn. Soc. Sci. Fish., 48, 1081–1088, 1982.

[3] A. Baskaran and M.C. Marchetti, *Nonequilibrium statistical mechanics of self-propelled hard rods*, J. Stat. Mech. Theory Exp., P04019, 2010.

[4] E. Bertin, M. Droz, and G. Grégoire, *Hydrodynamic equations for self-propelled particles: microscopic derivation and stability analysis*, J. Phys. A: Math. Theor., 42, 445001, 2009.

[5] F. Bolley, J.A. Cañizo, J.A. Carrillo, *Mean-field limit for the stochastic Vicsek model*, Appl. Math. Lett., 25, 339–343, 2011.

[6] H. Chaté, F. Ginelli, G. Grégoire, and F. Raynaud, *Collective motion of self-propelled particles interacting without cohesion*, Phys. Rev. E, 77, 046113, 2008.

[7] Y-L. Chuang, M.R. D'Orsogna, D. Marthaler, A.L. Bertozzi, and L. S. Chayes, *State transitions and the continuum limit for a 2D interacting, self-propelled particle system*, Physica D, 232, 33–47, 2007.

[8] I.D. Couzin, J. Krause, R. James, G.D. Ruxton, and N.R. Franks, *Collective memory and spatial sorting in animal groups*, J. theor. Biol., 218, 1–11, 2002.

[9] F. Cucker and S. Smale, *Emergent behavior in flocks*, IEEE T. Automat. Contr., 52, 852–862, 2007.

[10] P. Degond, A. Frouvelle, and J-G. Liu, *Macroscopic limits and phase transition in a system of self-propelled particles*, J. Nonlinear Sci. 23, 427–456, 2013.

[11] P. Degond, A. Frouvelle, and J-G. Liu, *Phase transitions, hysteresis, and hyperbolicity for self-organized alignment dynamics*, Arch. Ration. Mech. An., 216, 63–115, 2015.

[12] P. Degond, J-G. Liu, S. Motsch, and V. Panferov, *Hydrodynamic models of self-organized dynamics: derivation and existence theory*, Methods Appl. Anal., 20, 89–114. 2013.

[13] P. Degond and S. Motsch, *Continuum limit of self-driven particles with orientation interaction*, Math. Models Methods Appl. Sci., 18 Suppl., 1193–1215, 2008.

[14] P. Degond, P.F. Peyrard, G. Russo, and P. Villedieu, *Polynomial upwind schemes for hyperbolic systems*, C. R. Acad. Sci. Paris, Ser I, 328, 479–483, 1999.

[15] H. Fehske, R. Schneider, and A. Weisse, *Computational Many-Particle Physics*, Springer Verlag, 2007.

[16] A. Frouvelle, *A continuum model for alignment of self-propelled particles with anisotropy and density-dependent parameters* , Math. Mod. Meth. Appl. Sci., 22, 1250011, 2012.

[17] G. Grégoire and H. Chaté, *Onset of collective and cohesive motion* , Phys. Rev. Lett., 92, 025702, 2004.

[18] S. Henkes, Y. Fily, and M.C. Marchetti, *Active jamming: Self-propelled soft particles at high density*, Phys. Rev. E, 84, 040301, 2011.
[19] J.P. Hernandez-Ortiz, P.T. Underhill, and M.D. Graham, *Dynamics of confined suspensions of swimming particles*, J. Phys. Condens. Matter, 21, 204107, 2009.
[20] R.W. Hockney and J.W. Eastwood, *Computer Simulation Using Particles*, Institute of Physics Publishing, 1988.
[21] D.L. Koch and G. Subramanian, *Collective hydrodynamics of swimming microorganisms: Living fluids*, Annu. Rev. Fluid Mech., 43, 637–659, 2011.
[22] A. Mogilner, L. Edelstein-Keshet, L. Bent, and A. Spiros, *Mutual interactions, potentials, and individual distance in a social aggregation*, J. Math. Biol., 47, 353–389, 2003.
[23] S. Motsch and L. Navoret, *Numerical simulations of a non-conservative hyperbolic system with geometric constraints describing swarming behavior*, Multiscale Model. Simul., 9, 1253–1275, 2011.
[24] S. Motsch and E. Tadmor, *A new model for self-organized dynamics and its flocking behavior*, J. Stat. Phys., 144, 923–947, 2011.
[25] T.J. Pedley, N.A. Hill, and J.O. Kessler, *The growth of bioconvection patterns in a uniform suspension of gyrotactic micro-organisms*, J. Fluid. Mech., 195, 223–237, 1988.
[26] F. Peruani, A. Deutsch, and M. Bär, *Nonequilibrium clustering of self-propelled rods* , Phys. Rev. E, 74, 030904(R), 2006.
[27] V.I. Ratushnaya, D. Bedeaux, V.L. Kulinskii, and A.V. Zvelindovsky, *Collective behavior of self propelling particles with kinematic constraints: the relations between the discrete and the continuous description*, Phys. A, 381, 39–46, 2007.
[28] D. Saintillan and M.J. Shelley, *Instabilities, pattern formation and mixing in active suspensions*, Phys. Fluids., 20, 123304, 2008.
[29] B.Szabó, G.J Szöllösi, B. Gönci, Z. Jurányi, D. Selmeczi, and T. Vicsek *Phase transition in the collective migration of tissue cells: Experiment and model*, Phys. Rev. Lett, 74, 061908, 2006.
[30] J. Toner, Y. Tu, and S. Ramaswamy, *Hydrodynamics and phases of flocks,* Ann. Phys. - New York, 318, 170–244, 2005.
[31] T. Vicsek, A. Czirók, E. Ben-Jacob, I. Cohen, and O. Shochet, *Novel type of phase transition in a system of self-driven particles*, Phys. Rev. Lett., 75, 1226–1229, 1995.
[32] T. Vicsek and A. Zafeiris, *Collective motion*, Phys. Rep., 517, 71–140, 2012.
[33] F.G. Woodhouse and R.E. Goldstein, *Spontaneous circulation of confined active suspensions* , Phys. Rev. Lett., 109, 168105, 2012.